Supporting Information for:

Identification of structural changes in $CaCu_3Ti_4O_{12}$ on high energy ball milling and their effect on photocatalytic performance

Section S1 cumulative kinetic energy released during high energy ball milling

Considering the work done by N. Burgio et. al., [1] and revisited by G.-J. Lee et. al., [2], several kinetic parameters have to be considered to quantify the cumulative kinetic energy transferred to CCTO powders during high energy ball milling and ensure the formation of nanopowders. A brief description of the methodology and equations used is given below. The calculated kinetic parameters used in this work are reported in Table S1:

- the ball impact energies ΔE_b (mJ/hit) (Equation S1) and the ball impact frequency of the milling bodies v_t (s^{-1}) (Equation S2), were calculated as follow:

$$\Delta E_b = \frac{1}{2} \cdot \left(\rho_b \frac{\pi \cdot d_b^3}{6} \right) \cdot W_p^2 \cdot \left[\left(\frac{W_v}{W_p} \right)^2 \cdot \left(\frac{D_v - d_b}{2} \right)^2 \cdot \left(1 - 2 \cdot \frac{W_v}{W_p} \right) - 2 \cdot R \cdot (\quad)^2 \right] \quad (1)$$

$$v_t = N_b \cdot K \cdot (W_p - W_v) \qquad (2)$$

where ρ_b is the balls density, d_b is the balls diameter, W_p is the rotational angular speed of the supporting disk, W_v is the rotational angular speed of the vial, D_v is the diameter of the vial, R_p is the distance between the rotational axes, N_b is the balls number, K is a constant dependent on the milling set up.

- the obstacle factor Φ_b (Equation S3) takes into account the collisions between milling bodies which decrease the energy of each impact in the system was calculated as follow,

$$\Phi b = \frac{Vs}{Vjar} \qquad (3)$$

where V_s is the sum of powders, milling bodies and solvent volume and V_{jar} is the volume of the empty jar. This allows to obtain a more correct value of ball impact energy value $\Delta E_b{'}$ (mJ/hit) (Equation S4):

$$\Delta E_b{'} = \Phi b \cdot \Delta E_b \qquad (4)$$

- the cumulative kinetic energy supplied to the powders throughout the process ΔE_{cum} (kJ/g)

$$\Delta E_{cum} = \frac{\Delta E_b{'} \cdot v_t \cdot t}{m_p}$$

(Equation S5) was calculated as $\qquad (5)$

where t is the total milling time and m_p the powder weight.

Table S1. Kinetic parameters considered during high energy ball milling of CCTO powders

Φ_b	ΔE_b *(mJ/hit)*	$\Delta E_b{}'$ *(mJ/hit)*	v_t *(s^{-1}) · 10^5*	ΔE_{cum}*(kJ/g) · 10^4*
0,89	2,52	2,24	10,8	4,64

Section S2 experimental details on XPS analysis

XPS analysis was performed with a Φ-5600-ci spectrometer (Perkin-Elmer) using Mg Kα radiation. The sample analysis area was 800 μm in diameter. Survey scans were obtained in the 0–1100 eV range (187.8 eV pass energy, 0.8 eV step-1, 0.05 s step-1). Detailed scans were recorded for selected elements (23.5 eV pass energy, 0.1 eV step-1, 0.1 s step-1). The standard deviation for the Binding Energies (BEs) values is ± 0.2 eV. The BE shifts were corrected by assigning to the C1s peak associated with adventitious hydrocarbons a value of 284.8 eV. The atomic compositions were evaluated from peak areas using sensitivity factors supplied by Perkin-Elmer, taking into account the geometric configuration of the apparatus. The experimental uncertainty on the reported atomic composition values does not exceed ± 5% [3,4].

Table S2. Elemental analyses expressed as the M/Ti (M=Ca, Cu, Zr) *ratio detected by ICP-OES*

CCTO			
	Ca/Ti	Cu/Ti	Zr/Ti
Theoretical	0.250	0.750	/
Experimental	0.235(3)	0.765(4)	/
CCTO-GM			
	Ca/Ti	Cu/Ti	Zr/Ti
Theoretical	0.250	0,750	/
Experimental	0.228(9)	0.741(18)	0.031(12)

Table S3. Ti k-edge EXAFS fitting for CCTO and CCTO-GM

Sample	Path	Coordination number[i]	Path length (Å)	$2\sigma^2$(Å^2)	ΔE (eV)	R-factor
CCTO	Ti-O	6(1)	1.93(1)	0.003(2)	-5(3)	0.067
	Ti-Cu[ii]	6	3.3(2)	0.005(2)		
	Ti-Ca[ii]	2				
CCTO-GM	Ti-O	7(2)	1.92(2)	0.007(5)	4(4)	0.085
	Ti-Cu[ii]	6	3.23(3)	0.009(3)		
	Ti-Ca[ii]	2				

Fitting parameters: 3.2 <k< 9 and 1<R< 4. (i) S_0^2 values (fitted from TiO_2) fixed at 0.65 and CN values fixed. (ii) Cu and Ca path lengths and $2\sigma^2$ values linked together.
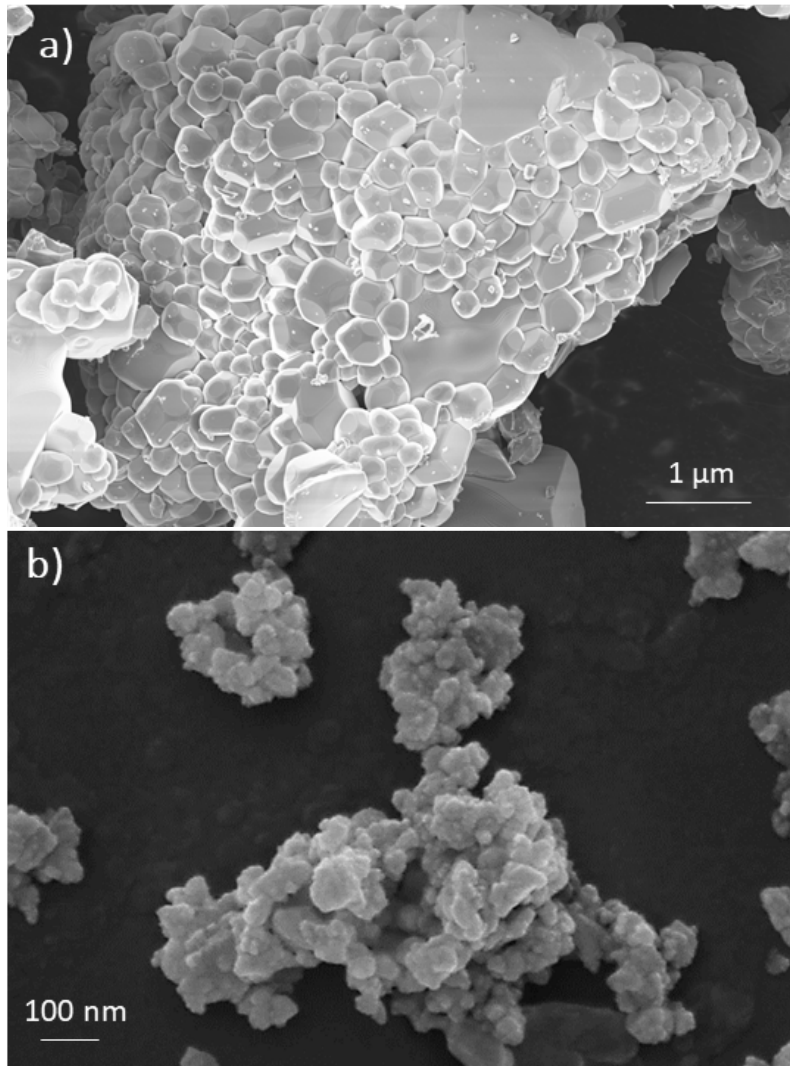
Figure S1. SEM micrographs of CCTO a) and CCTO-GM b) powders.

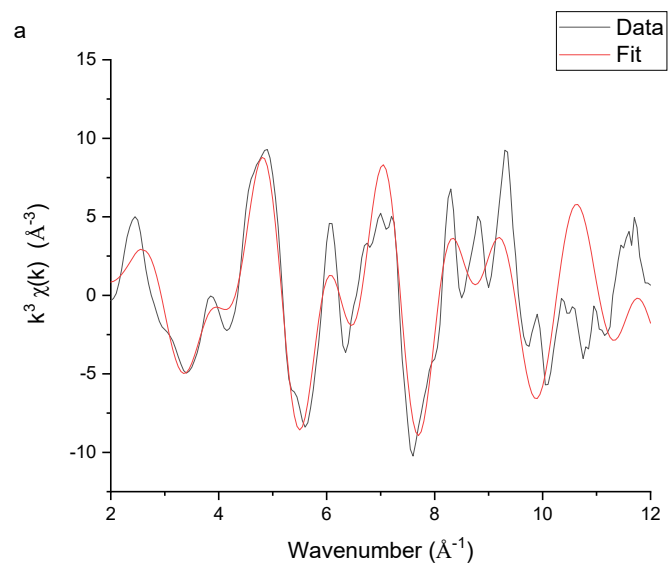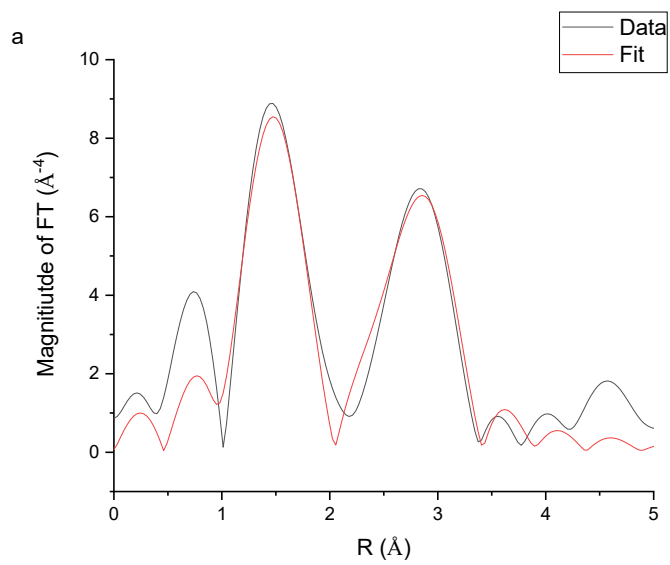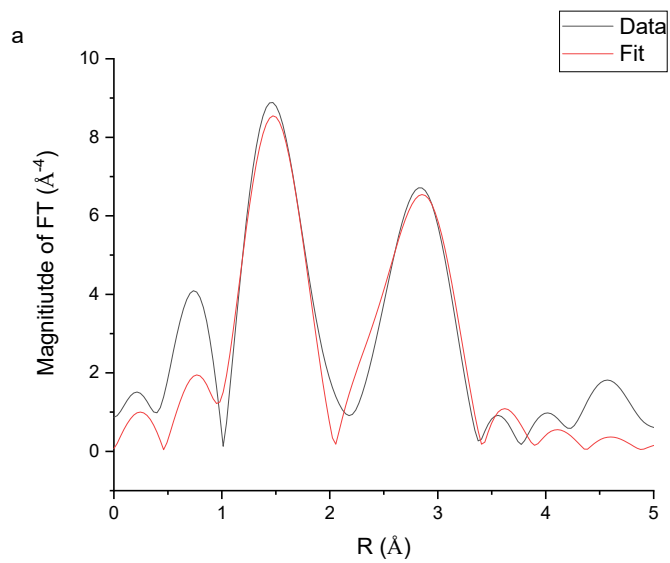*Figure S2. K space EXAFS fitting of Ti-ledge data for CCTO (a) and CCTO-GM (b)*
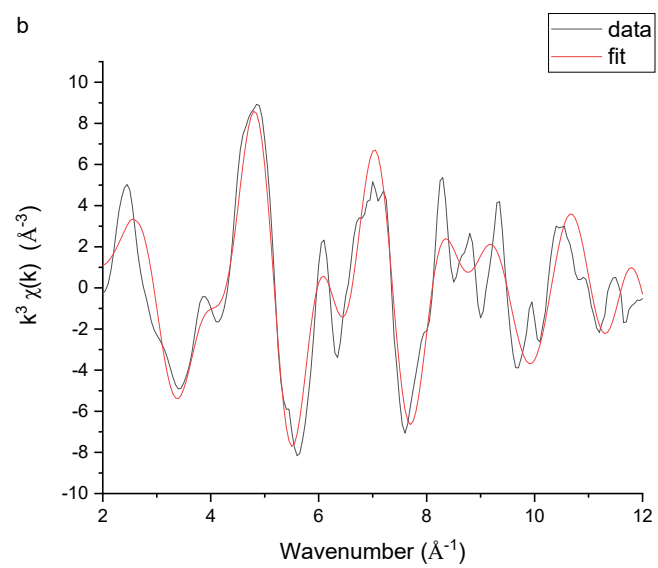
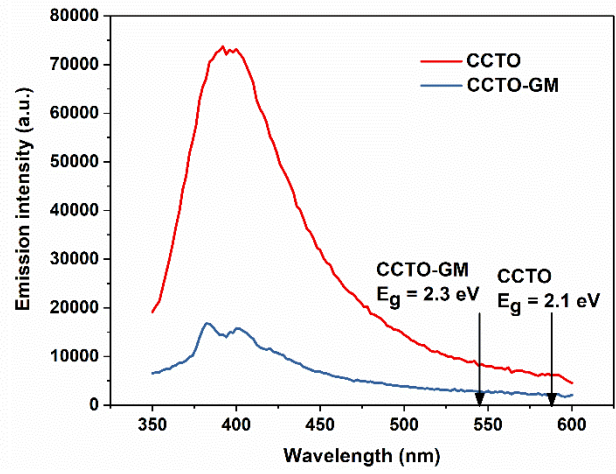*Figure S3. R space EXAFS fitting of Ti-ledge data for CCTO (a) and CCTO-GM (b)*
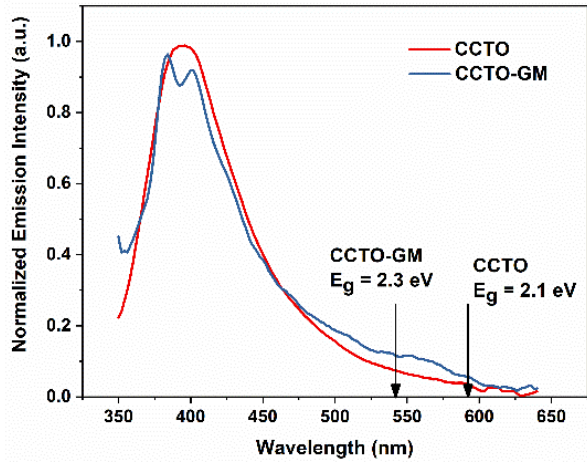
Figure S4. Photoluminescence (PL) spectra excited at 380 nm. Left normalised and right unnormalised spectra
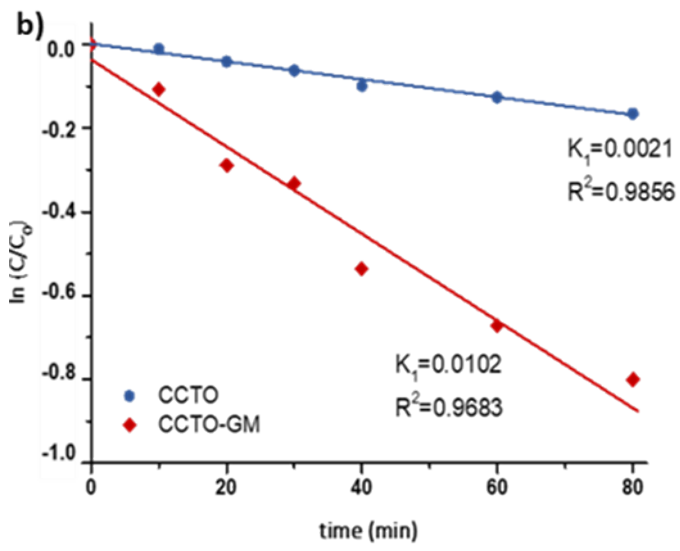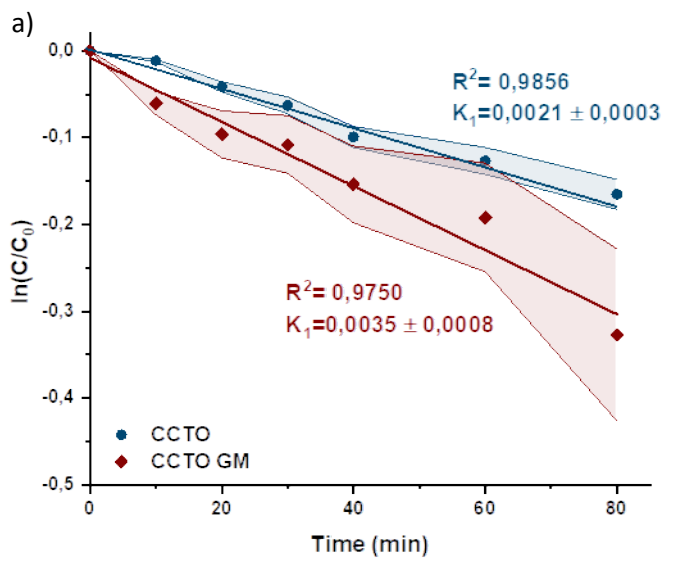
Figure S5. First order kinetic decay plot with error bands

related to photodegradation tests with equivalent surface area (a) or mass (b)- 100 mg.
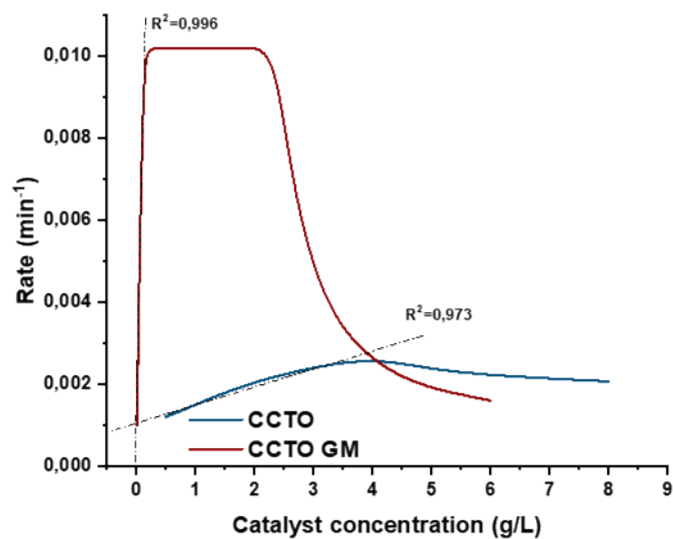

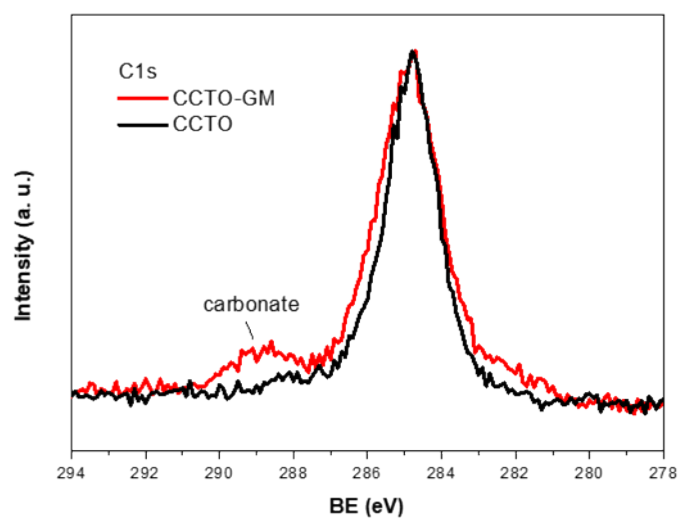*Figure S6. Dependence of reaction rate on photocatalyst concentration.*

Figure S7. High resolution C1s region for CCTO and CCTO-GM samples.

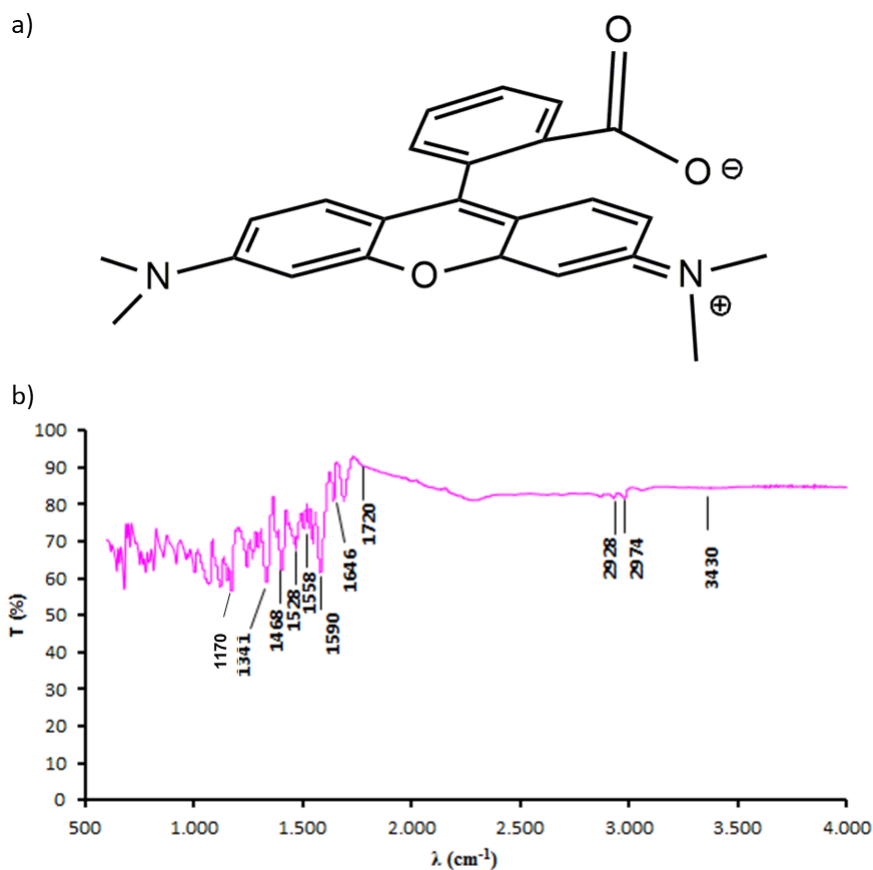## Section S3 Structure and ATR-FTIR spectrum of Rhodamine B

a)

b)

Figure S8. Rhodamine B structure (a) and related FT-IR spectrum of Rhodamine B commercial powders (b).

Table S4. IR band position of the characteristic Rhodamine B peaks [5].

Wavenumber (cm^{-1})	Characteristic vibrations
3430	Stretching -OH
2974	Stretching -CH2-
2928	Stretching C–CH3
1720	Stretching C=O
1646	Bending C-N
1590	Aromatic C-C stretching
1558-1530	Heterocyclic C-C stretching
1528	Aromatic C-C stretching
1468	Aromatic C-C stretching
1341	Bending C-arile
1170-1050	Stretching C-OH

Section S4 ATR-FTIR curve fitting

The deconvolution of CCTO spectrum after dark and photodegradation reaction in the spectral range 900 - 1500 cm^{-1} is reported in Figure S9 [6,7]. The spectrum is fitted with increasing Gaussian components using OriginPro 9.0 software (OriginLab Co., Northampton, MA) monitoring the adjusted R^2 and χ^2 and selecting the number of components that minimize χ^2 and makes R^2 closer to 1. As shown in Figure S9 a) and b), the number of Gaussian components that best fit both spectra are 3. In Figure S9 c) and d) are reported the FTIR spectra fitting with 3 gaussian components. To further support the results obtained by the iterative curve fitting (29 iterations), the number of sub-bands and their position were also determined by performing the second derivative curve of the FTIR spectra [6,8], followed by smoothing with the Savitsky–Golay function with polynomial order of 2. As shown in Figure S9 e and f, the second derivative led to the same number of sub-bands and peak positions are very similar (± 1 cm^{-1}) to the ones reported for the deconvolution procedure.
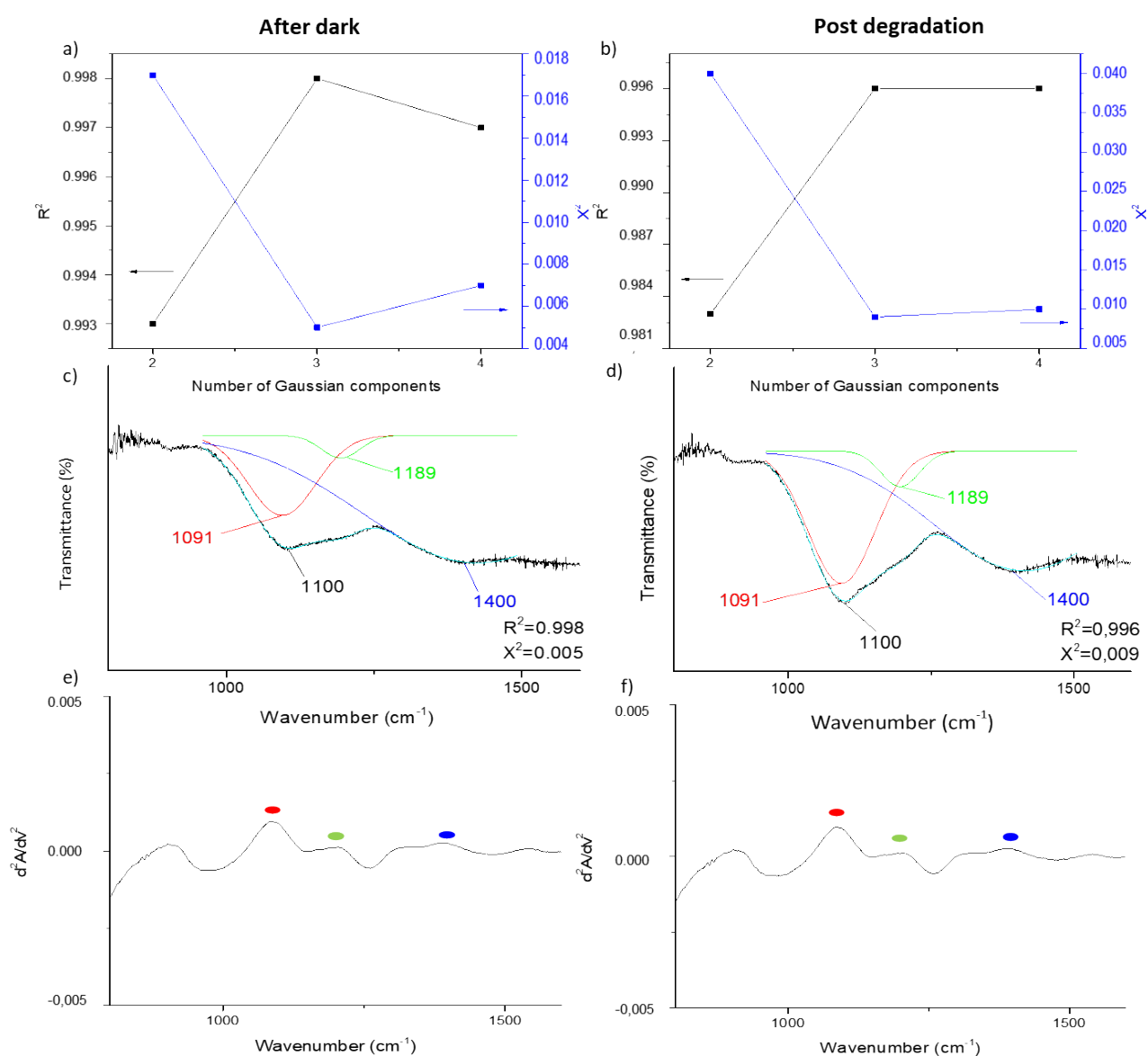

Figure S9. Plots of R^2 and χ^2 vs number of Gaussian components (a-b), fitted FTIR spectra with 3 gaussian components (c-d) and 2nd derivative curve for the FTIR spectrum (e-f) after dark (Figures on the left) and after photodegradation reaction (Figures on the right).

Section S5 Rhodamine B adsorption:

The molecules adsorption coordination on the photocatalyst's surface greatly influences the organics degradation [9,10]. It is well known that xantene dyes self-dimerize in solution even in low concentration (typically > $5 \cdot 10^{-6}$ M) [11,12]. Photocatalytic tests are conducted using a $5.2 \cdot 10^{-6}$ M Rhodamine B solution, therefore can be supposed that the main species present in the liquid media is the monomer [11]. Considering that both samples show a negatively charged surface, dye molecules could interact with CCTO through their xantene group (positively charged) [13], as schematically shown in Figure S10 a). The aggregation of monomers adsorbed onto CCTO and CCTO-GM surface can be excluded since no shifts of the main UV-Vis absorption peak of RhB (554 nm) is highlighted after one hour of stirring in dark condition, as shown in Figure S10 b) [9].
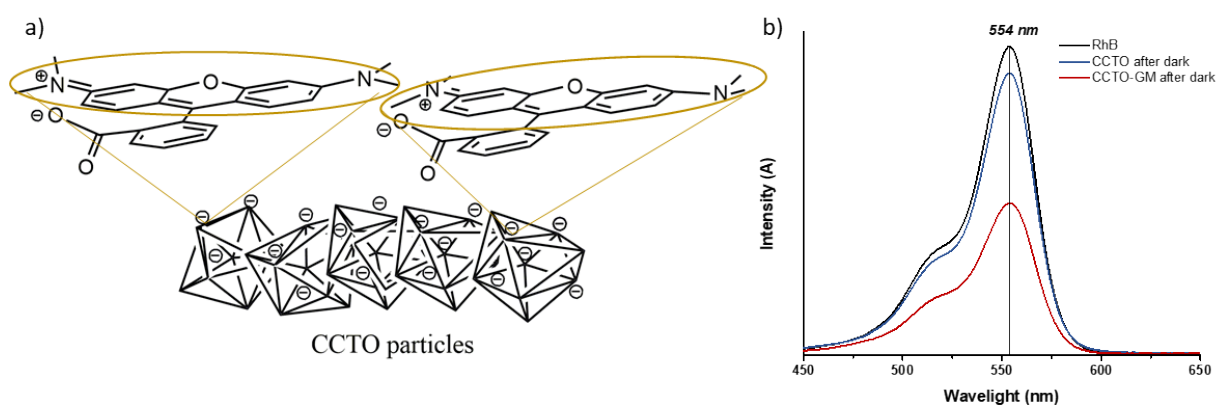

Figure S10. a) Schematic representation of Rhodamine B adsorption on calcium copper titanate photocatalyst's; b) UV-Vis absorption spectra collected for the pure rhodamine solution and after one hour of stirring in dark with CCTO and CCTO-GM.

Supporting Information's References

1 N. Burgio, A. Iasonna, M. Magini, S. Martelli, F. Padella Mechanical Alloying of the Fe-Zr System. Correlation between Input Energy and End Product, *Il Nuovo cimento D, 1991,* **13**, 459–476.

2 G.-J. Lee, E.-K. Park, S.-A Yang, J.-P. Park, S.-D. Bu, K. Lee, Rapid and direct synthesis of complex perovskite oxides through a highly energetic planetary milling, *Scientific Reports,* 2017, DOI: 10.1038/SREP46241.

3 D.B. Dell'Amico, H. Bertagnolli, F. Calderazzo, M. D'Arienzo, S. Gross, L. Labella, M. Rancan, R. Scotti, B.M. Smarsly, R. Supplit, E. Tondello, E. Wendel, Nanostructured Copper Oxide on Silica–Zirconia Mixed Oxides by Chemical Implantation, *Chemistry – A European Journal*, 2009, **15**, 4931–4943.

4 M.G. Pelizzo, A.J. Corso, E. Tessarolo, R. Böttger, R. Hübner, E. Napolitani, M. Bazzan, M. Rancan, L. Armelao, W. Jark, D. Eichert, A. Martucci, Morphological and Functional Modifications of Optical Thin Films for Space Applications Irradiated with Low-Energy Helium Ions, *ACS Appl. Mater. Interfaces*, 2018, **10**, 34781–34791.

5 LI Jing-yi, MA Wan-hong, LEI Peng-xiang, ZHAO Jin-cai Detection of intermediates in the TiO2-assisted photodegradation of Rhodamine B under visible light irradiation, *Journal of Environmental Sciences*, 2007, **19**, 892–896.

6 C. Branca, A. Arcovito, E. Cosio, M. Interdonato, G. Sabatino, U. Wanderlingh, G. D'Angelo Combining Fourier transform infrared and Raman spectroscopies with Gaussian deconvolution: An improved approach for the characterization of emeralds, *J Raman Spectrosc*, 2020, **51**, 693–701.

7 C. Branca, G. D'Angelo, C. Crupi, K. Khouzami, S. Rifici, G. Ruello, U. Wanderlingh Role of the OH and NH vibrational groups in polysaccharidenanocomposite interactions: A FTIR-ATR study on chitosan and chitosan/clay films, *Polymer, 2016,* **99**, 614–622.

8 A. Sadat, I. J. Joye Peak Fitting Applied to Fourier Transform Infrared and Raman Spectroscopic Analysis of Proteins, *Appl. Sci*, 2020, DOI: 10.3390/APP10175918.

9 K. Adachi, K. Watanabe, S. Yamazaki, pH-Responsive Switchable Aggregation Phenomena of Xanthene Dyes Adsorbed on Tungsten(VI) Oxide Colloid Surface, *Ind Eng Chem Res,* 2014, **53**, 13046–13057.

10 J. Zhao, T. Wu, K. Wu, K. Oikawa, H. Hidara, N. Serpone Photoassisted Degradation of Dye Pollutants. 3. Degradation of the Cationic Dye Rhodamine B in Aqueous Anionic Surfactant/TiO2 Dispersions under Visible Light Irradiation: Evidence for the Need of Substrate Adsorption on TiO2 Particles, *Environ Sci Technol,* 1998, **32**, 2394–2400.

11 W. West, S. Pierce The Dimeric State of Cyanine Dyes, *The Journal of Physical Chemistry*, 1965, DOI: 10.1021/J100890A019.

12 L. Arbeloa, P. R. Ojeda Dimeric state of Rhodamine B, *Chemical Physics Letters,* 1982, **87**, 556–560.

13 D. Glossman-Mitnik Computational Study of the Chemical Reactivity Properties of the Rhodamine B Molecule, *Procedia Computer Science,* 2013, **18,** 816–825.